

Development of Iron-Doped Hydroxyapatite Coatings

Daniela Predoi ^{1,*}, Simona Liliana Iconaru ¹, Steluta Carmen Ciobanu ¹, Silviu-Adrian Predoi ^{2,3}, Nicolas Buton ⁴, Christelle Megier ⁴ and Mircea Beuran ^{5,6,*}

¹ National Institute of Materials Physics, Atomistilor Street, No. 405A, P.O. Box MG 07, 077125 Magurele, Romania; simonaiconaru@gmail.com (S.L.I.); ciobanucs@gmail.com (S.C.C.)

² Polytech Sorbonne, Sorbonne Universite, 4 Place Jussieu, 75005 Paris, France; silviuadrian00@gmail.com

³ Lycée Louis-le-Grand, 123 Rue Saint-Jacques, 75005 Paris, France

⁴ HORIBA Jobin Yvon S.A.S., 6-18, Rue du Canal, 91165 Longjumeau CEDEX, France; nicolas.buton@horiba.com (N.B.); christelle.megier@horiba.com (C.M.)

⁵ Department of Surgery, Carol Davila University of Medicine and Pharmacy, 8 Eroii Sanitari, Sector 5, 050474 Bucharest, Romania

⁶ Emergency Hospital Floreasca Bucharest, 8 Calea Floresca, 014461 Bucharest, Romania

* Correspondence: dpredoi@gmail.com (D.P.); beuranmircea@gmail.com (M.B.)

Abstract: It is known that iron is found as a trace element in bone tissue, the main inorganic constituent of which is hydroxyapatite. Therefore, iron-doped hydroxyapatite (HApFe) materials could be new alternatives for many biomedical applications. A facile dip coating process was used to elaborate the iron-doped hydroxyapatite (HApFe) nanocomposite coatings. The HApFe suspension used to prepare the coatings was achieved using a co-precipitation method, which was adapted in the laboratory. The quality of the HApFe suspension was assessed through dynamic light scattering (DLS), ultrasonic measurements, and zeta potential values. The hydroxyapatite XRD patterns were observed in the HApFe nanocomposite with no significant shifting of peak positions, thus suggesting that the incorporation of iron did not significantly modify the hydroxyapatite structure. The morphology of the HApFe nanoparticles was evaluated using transmission electron microscopy (TEM). Scanning electron microscopy (SEM) was used in order to investigate the morphologies of HApFe particles and coatings, while their chemical compositions were assessed using energy-dispersive X-ray spectroscopy (EDS). The SEM results suggested that the HApFe consists mainly of spherical nanometric particles and that the surfaces of the coatings are continuous and homogeneous. Additionally, the EDS spectra highlighted the purity of the samples and confirmed the presence of calcium, phosphorous, and iron in the analyzed sample. The in vitro cytotoxicity of the HApFe suspensions and coatings was evidenced using osteoblast cells. The MTT assay showed that both the HApFe suspensions and coatings exhibited biocompatible properties.

Keywords: iron; hydroxyapatite; ultrasound measurement; suspension; coatings; cell viability



Citation: Predoi, D.; Iconaru, S.L.; Ciobanu, S.C.; Predoi, S.-A.; Buton, N.; Megier, C.; Beuran, M. Development of Iron-Doped Hydroxyapatite Coatings. *Coatings* **2021**, *11*, 186. <https://doi.org/10.3390/coatings11020186>

Academic Editor: Mazeyar Parvinzadeh Gashti
Received: 30 December 2020
Accepted: 1 February 2021
Published: 5 February 2021

Publisher's Note: MDPI stays neutral with regard to jurisdictional claims in published maps and institutional affiliations.



Copyright: © 2021 by the authors. Licensee MDPI, Basel, Switzerland. This article is an open access article distributed under the terms and conditions of the Creative Commons Attribution (CC BY) license (<https://creativecommons.org/licenses/by/4.0/>).

1. Introduction

Advances in nanotechnology have allowed the development of new nanometer-sized materials, which due to their superior properties can be used in the field of biomedicine [1]. Recently, studies have shown that superparamagnetic nanoparticles (magnetite (Fe₃O₄) or maghemite (γ-Fe₂O₃)) can be successfully used in applications such as medical imaging (MRI) [2], drug delivery [3], and cancer therapy [4]. The use of these new types of materials as drug delivery systems has many benefits and advantages (better pharmacokinetics, diminished side effects, etc.) [5–7].

At the same time, small amounts (traces) of iron are found in bone tissue, and studies have shown that iron can accelerate tissue regeneration [8]. On the other hand, one of the most investigated synthetic bioceramic materials with applications in tissue engineering and biomedical field is hydroxyapatite (HAp, [Ca₁₀(PO₄)₆(OH)₂]) [9]. Hydroxyapatite is the main inorganic constituent in bones and teeth. Moreover, its excellent biological

properties (biocompatibility, bioactivity, osteoconductivity, etc.), together with its physico-chemical properties, make it suitable for applications in many fields [10–14]. Due to its flexible and unique structure, HAp allows a large number of substitutions with various ions (e.g., Fe, Ag, Zn, etc.) [11,14–16]. Previous studies have shown that these substitutions improve the physico-chemical and biological properties of pure HAp [11,15,16].

Currently, the accumulation of iron in bone tissue is not fully understood, but there are studies that have shown that iron deficiency can lead to inhibition of osteoblast cell mineralization (in vitro tests) [15,17]. However, as the use of iron oxide nanoparticles in biomedical applications is not possible due to the rapid aggregation of nanoparticles under physiological conditions, the development of magnetic hydroxyapatite (iron or iron oxide–hydroxyapatite, HApFe) nanobiocomposites is of real interest [18,19]. Therefore, the presence of HAp on the surfaces of iron oxide nanoparticles improves both their stability and biocompatibility. Moreover, the presence of HAp facilitates the adhesion of various therapeutic molecules on the surfaces of nanocomposites [18,20]. Ajeesh et al. [21] pointed out in their study that HApFe nanocomposites exhibit improved radiopacity compared to HAp. Additionally, Panseri et al. [15] and Pareta et al. [22] highlighted an improvement in osteoblast cell proliferation in the presence of nanobiocomposites. The bioactivity of HAp is improved by the presence of iron in the HAp structure, which was proven by the in vitro studies conducted by Chandra et al. [20]. Additionally, the in vivo studies conducted on the magnetic HAp scaffolds showed that the bone formation and biocompatibility were not affected in the short term by their magnetization [23]. Furthermore, magnetic HAp scaffolds have been proven to be promising materials that could promote rapid formation of mature bone [24]. The iron concentration plays an important role in the properties of magnetic HAp. It has been observed that with increasing Fe^{3+} concentration, the crystallite size and crystallinity decrease, the morphology of the particles change from spherical to rods, and the magnetic properties change from diamagnetic (for HAp) to superparamagnetic (for the iron-substituted HAp) [20,25]. It was also observed that the drug release profile varies depending on the Fe content of the sample, with studies showing that 100% drug release was achieved after 6 h in the case of HAp, while 100% drug release was obtained after 9, 12, and 18 h for Fe-substituted hydroxyapatite samples of varying Fe content (the shortest time being obtained for samples with an increased Fe content loaded with 5 Fluorouracil) [20].

HApFe nanocomposites can be synthesized using various techniques, including coprecipitation [26], hydrothermal methods [27], spray-drying [28], and high-energy ball milling [29]. An important problem that arises when hydroxyapatite is used as a coating for implants is that of implant failure, which is mainly due to the low stability of HAp under physiological environments [30–32]. Therefore, the presence of iron or iron oxide can increase the stability of hydroxyapatite layers [16,31]. Thus, the applicability of these new materials with superior properties could be extended. On the other hand, other studies [20] have demonstrated that after the immersion of HApFe in simulated body fluid (SBF) for 3 weeks, the best bone-bonding ability (quantified by the presence of an apatite layer on the pellets surfaces) was obtained for Fe-doped hydroxyapatite as compared to HAp. In previous studies, the blood compatibility of magnetic HAp samples has been proven [20,33,34].

Studies conducted on HApFe obtained using the neutralization method revealed that concomitant addition of Fe^{2+} and Fe^{3+} ions under specific synthesis conditions resulted in materials with close (Fe + Ca)/P ratio values to the theoretical (Ca/P = 1.67) [35]. The same studies [35] reported superparamagnetic properties for HApFe samples with a small content of Fe_3O_4 . In this context, the novelty of our study is in presenting for the first time information regarding the stability and homogeneity of HApFe suspensions obtained via the correlation of dynamic light scattering (DLS), ultrasonic, and zeta potential measurements. Additionally, we provide new information regarding the cytotoxicity of iron-doped hydroxyapatite solutions and coatings using osteoblast cells. Through this study, we aim to contribute to the better understanding of the stability, structure,

morphology, chemical composition, and cytotoxicity of the synthesized samples (HApFe solutions and coatings).

The aim of this study is to highlight the stability of the iron-substituted hydroxyapatite suspensions used in the creation of thin layers, which could be used in various medical applications. The crystal structure of the HApFe nanocomposite powder obtained from the suspension, the morphology of the nanoparticles in suspension, and the coating surface are also assessed. The morphology of the HApFe particles is investigated using scanning electron microscopy and transmission electron microscopy. The presence of Fe, Ca, P, and O are highlighted using EDS studies. The in vitro cytotoxicity of the HApFe suspensions and coatings is shown using osteoblast cells. The MTT assay highlights that both the HApFe suspensions and coatings exhibit excellent biocompatible properties.

2. Materials and Methods

2.1. Materials

Iron-doped hydroxyapatite (HApFe) was produced using $\text{Ca}(\text{NO}_3)_2 \cdot 4\text{H}_2\text{O}$ (calcium nitrate tetrahydrate; Sigma Aldrich, St. Louis, MO, USA, $\geq 99.0\%$), $\text{Fe}(\text{NO}_3)_3 \cdot 9\text{H}_2\text{O}$ (Iron(III) nitrate nonahydrate; Merck, Kenilworth, NJ, USA, $\geq 99.95\%$), $(\text{NH}_4)_2\text{HPO}_4$ (ammonium hydrogen phosphate; Sigma Aldrich, St. Louis, MO, USA, $\geq 99.0\%$), ammonium hydroxide (NH_4OH) (Thermo Fisher Scientific, Waltham, MA, USA), and de-ionized water.

2.2. Iron-Doped Hydroxyapatite (HApFe) Suspensions

In order to obtain the iron-doped hydroxyapatite (HApFe), 0.16 M of $\text{Ca}(\text{NO}_3)_2 \cdot 4\text{H}_2\text{O}$ aqueous solution and 0.05 M of $\text{Fe}(\text{NO}_3)_3 \cdot 9\text{H}_2\text{O}$ aqueous solution were coprecipitated in 0.1 M of $(\text{NH}_4)_2\text{HPO}_4$ aqueous solution under continuous stirring for 4 h at 100 °C. The pH was monitored during the synthesis and adjusted to 10 by adding ammonium hydroxide solution (1:1) drop-by-drop. The resulting suspension was filtered and washed 5 times and redispersed in de-ionized water (100 mL). The HApFe suspension was continuously stirred for 12 h at 40 °C. The resulting HApFe suspension was analyzed using different techniques.

2.3. Thin Layer of HApFe

The dip coating process [36], a facile and economical technique, was used in order to prepare the HApFe coatings. The substrate material used in this study was the Si. Through this process, the HApFe suspension was used to obtain the coatings. The Si substrate was washed with ethanol. Four successive layers of HApFe were deposited in the same way. Each layer was dried at 80 °C for 4 h. The resulting coating was heat-treated at 300 °C for 1 h. A rate of 5 °C/min was set for cooling.

2.4. Characterization Methods

An SZ-100 Nanoparticle Analyzer from Horiba-Jobin Yvon (Horiba, Ltd., Kyoto, Japan) was used for both particle size analysis and zeta potential measurements (ZP). Particle size analysis was effectuated by dynamic light scattering (DLS). The sample measurements were taken at 25 ± 1 °C. To dilute the suspensions before analysis, the distilled water was used (0.4 mg Fe/mL).

Ultrasound measurements were conducted on a concentrated suspension obtained using the preparation process according to Prodan et al. [37]. Double-distilled water, being the most stable suspension, was considered the standard, which was prepared under the same experimental conditions. The stability of the analyzed suspension was related to that of the double-distilled water. Double-distilled water was the fluid used as the reference in evaluating the stability of the HApFe suspension. The information on the stability of the HApFe suspension is given using the evolution of the signals over time and attenuation vs. time. An exact determination of the ultrasonic velocity in the HApFe suspension for each signal was made by determining the delays between the first three echoes recorded for the

sample and the double-distilled water. The parameter “*s*” was calculated according to the formula $s = \frac{1}{A_m} \left| \frac{dA}{df} \right|$, where A_m represents the average amplitude of the signals.

X-ray diffraction (XRD) pattern data for the HApFe powder were recorded at room temperature using a Bruker D8 Advance diffractometer with nickel-filtered Cu K α ($\lambda = 1.5418 \text{ \AA}$) radiation (Billerica, MA, USA). The scanning range was 20°–60° in 2 θ with a step of 0.02° and a time per step of 0.4 s. In order to evaluate the crystal structure of the HApFe nanocomposite, the suspension was centrifuged. The resulting HApFe powder was dried for 12 h in an oven at 300 °C. The average crystal size of the HApFe nanocomposite powder and coating were calculated using the well-known Scherrer relationship [38]:

$$\Gamma = (0.94 \cdot \lambda) / (D \cos \theta) \quad (1)$$

where Γ is the full-width at half-maximum (FWHM), λ is the X-ray wavelength, D is the crystal size, and θ is the Bragg angle.

The morphology and particle size of the HApFe nanocomposite suspension were investigated using transmission electron microscopy (TEM) utilizing a CM 20 instrument (Philips FEI, Eindhoven, The Netherlands), which was equipped with a Lab6 instrument (works at 200 kV). The TEM analyses were conducted by dispersing the particle suspension in double-distilled water, after which a drop from the dispersion was dropped on the copper grid and dried under an infrared lamp before being examined. Here, 700 particles were measured to calculate the average particle size.

Scanning electron microscopy (SEM) was used to investigate the morphologies of HApFe and derived coatings with the aid of a Hitachi S4500 instrument (Hitachi, Tokyo, Japan). The quantitative elemental composition and elemental distribution maps were assessed with an EDAX (Ametek EDAX Inc., Mahwah, NJ, USA) using energy-dispersive X-ray spectroscopy (EDS). Before being studied using scanning electron microscopy (SEM), a drop of the colloidal suspension of the HA

pFe was placed on a double-sided adhesive carbon tape on the microscope support. It was then dried in a vacuum and subsequently placed on the microscope for investigation. The SEM micrographs (high-resolution) of HApFe samples were recorded at a magnification of $\times 100,000$ and 30 kV. EDS spectra were recorded using a collecting time of 180 s per measurement. Here, 700 particles were measured to calculate the average particle size (D_{SEM}). The thickness of the HApFe coatings was evaluated using field-emission scanning electron microscopy. The three-dimensional (3D) surface graphics of SEM images were obtained [39] using Image J software (ImageJ 1.51j8, National Institutes of Health, Bethesda, MD, USA).

Atomic force microscopy (AFM) was used to examine the HApFe coating surface morphology and roughness using a NT-MDT NTEGRA Probe Nano Laboratory instrument (NT-MDT, Moscow, Russia). The topography of the HApFe coating surface was obtained in non-contact mode with the aid of a silicon NT-MDT NSG01 cantilever coated with a 35 nm gold layer. The AFM topography was captured on a surface area of $10 \times 10 \mu\text{m}^2$, and the root mean square roughness (R_{RMS}) was also calculated. The AFM analysis were performed at $25 \pm 1 \text{ }^\circ\text{C}$ and the data analysis was performed using Gwyddion 2.55 software (Department of Nanometrology, Czech Metrology Institute, Brno, Czech Republic) [40].

2.5. Cell Viability Assay

The biocompatibility of both the iron-doped hydroxyapatite (HApFe) suspension and nanocomposite coatings was assessed using primary human osteoblast cells obtained from the upper part of a patient’s femur. The osteoblast cultures were designed according to the protocol previously reported in [41]. The cells were grown in Dulbecco’s modified Eagle’s medium (DMEM) supplemented with fetal bovine serum, DMEM sodium pyruvate, glutamine, and an antibiotic mix and incubated at 37 °C in a CO₂ atmosphere. After obtaining the osteoblast culture, the cells were treated with trypsin, seeded at a density of 10⁵ cells/mL in Petri dish, and incubated with the HApFe suspensions and coatings for different time intervals (24, 48, and 72 h). The coatings were sterilized and then placed

in Petri dishes for osteoblast cell implantation at a set density of 1×10^5 cells/cm². The cells were cultured on the surfaces of the HApFe coatings in “as-prepared” condition. The cultures were evaluated for cell viability at 24, 48, and 72 h (MTT assay). In contrast, osteoblast cells were seeded at the same density of 10^5 cells/mL in Petri dish and incubated with the iron-doped hydroxyapatite suspensions for the same time intervals. The control cell culture was grown on a polystyrene Petri dish. The cell viability was determined using the standard colorimetric assay MTT (3-(4, 5-dimethylthiazol-2-yl)-2,5-diphenyltetrazolium bromide) reduction test. The absorbance was quantified by measuring the wavelength at 595 nm using a TECAN spectrophotometer. In order to quantify the data, the value of the absorbance obtained for the control cell culture (culture grown on polystyrene Petri dish) was set as 100% viability and the other absorbance values were transformed to a % of viability in relation to the control sample. The cell adhesion on the surface of HApFe nanocomposite coatings was also assessed by AFM studies. For this purpose, after 24, 48, and 72 h of incubation of the coatings with the cell culture, the coatings were removed from the culture medium, washed with saline solution, and fixed with cold methanol. The cells were then post-fixed using osmium tetroxide and tannic acid.

For the in vitro experiments, three independent experiments were performed, each with three replicates. The data are presented as means \pm standard deviation (SD). Furthermore, paired and two-sample *t*-tests were used to perform the statistical analysis. Values of $p \leq 0.05$ were considered as statistically significant.

3. Results

In order to achieve uniform coatings using the dip coating process, the suspensions must be stable. As a result, one of our concerns was to achieve a stable HApFe suspension with biocompatible properties that could be used in various biomedical and industrial applications. The quality of the suspension used to make the coatings was analyzed using dynamic light scattering (DLS), ultrasonic measurements, and zeta potential values. Testing of the homogeneity of the HApFe suspension was necessary both to assess the deposits and for biological studies regarding the biocompatibility of the solution and the obtained coatings. The three techniques mentioned above are non-invasive and provide important information on the quality of the analyzed suspension. The advantages of the DLS technique are that the measurements are very fast and require small amounts of product to study the quality of the HApFe suspension. DLS measurements were performed on the HApFe suspension diluted 20 times. Reliable estimates of the quality of the HApFe suspension were obtained from DLS studies. The results of DLS studies on the particle size and distribution of the HApFe and the respective nanoparticles are presented in Figure 1. Figure 1a reveals DLS data weighted by numbers, while DLS data weighted by volume are presented in Figure 1b. The particle size analysis of the HApFe suspension showed a monomodal distribution. The average particle size of the HApFe was 57.09 nm when the DLS data were weighted by numbers (Figure 1a). The average particle size of the HApFe was 64.62 nm when the DLS data were weighted by volume (Figure 1b).

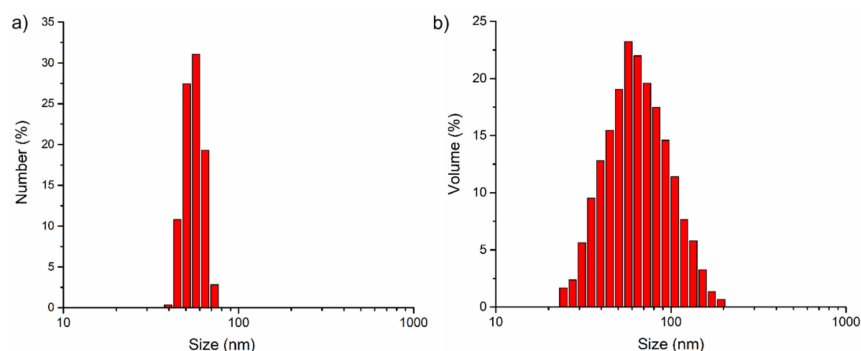


Figure 1. Dynamic light scattering (DLS) measurements of the size dispersion of the HApFe, showing data weighted by the number (a) and volume (b) of particles, respectively.

The value obtained for the zeta-potential (ZP) following the measurements was -39.9 mV. The behavior of the signals over time after sending the ultrasonic pulses through the HApFe suspension is presented in Figure 2a. Following the calculations, the ultrasonic velocity in the HApFe suspension was $c = 1531.26$ m/s, while in the double-distilled water the value of the ultrasound speed was $c_0 = 1496.19$ m/s. Both for the HApFe suspension and for the reference fluid, the measurements were performed at 24.8 °C. As can be seen, the ultrasound velocity through the sample and through the reference fluid shows negligible variation during the experiment. Figure 2b shows the maximum amplitudes of the transmitted signals vs. recording moments. The constant amplitudes of all three recorded signals are clearly shown in Figure 2b. Following the analysis of the signals, it was found that the first echo measured gave the highest accuracy. The slope of the maximum amplitude of the transmitted signal vs. recording moments in the case of the first echo was $s = 3 \times 10^{-6}$ (1/s). For double-distilled water (considered as reference) $s = 0$, the value of the parameter “s” calculated for the first echo revealed the good stability of the HApFe suspension. The stability of the HApFe suspension was also highlighted in the frequency spectrum of the first transmitted echo relative to the reference fluid (Figure 2c). After recording 950 signals over 5000 s, a very good overlap was observed, showing the remarkable stability of the HApFe suspension. The 4 MHz maximum output is a feature of transducers. Spectral amplitudes of relative variation vs. time during the experiment provided information on the stability of the HApFe suspension. Figure 2d shows the spectral amplitudes of relative variation vs. time for the first echo. The initial highest amplitude ratio of 0.93 was observed at 2 MHz, while the lowest amplitude ratio equal to 0.79 was observed at 8 MHz. Knowing these relative amplitudes, we were able to compute the attenuation of the signals. The averaged attenuation of the first echo across the whole experiment showed increasing values for higher frequencies (Figure 2e) compared to the same dependency on frequency for the reference fluid. The attenuation was considerably higher (2.8–11 nepper/m) for the sample compared to the reference fluid (0.3–1.3 nepper/m for). The attenuation for each spectral component can also depend strongly on the moment during the experiment, as was shown by the authors for other samples [42,43]. For this case (Figure 2f), there is a weak variation for each spectral amplitude. The amplitudes at lower frequencies (e.g., 2 MHz) are constant or slowly increase over time. On the contrary, at higher frequencies (e.g., 8 MHz), slowly decreasing amplitudes can be observed, being more sensitive to the agglomerations of particles that gradually form during slow sedimentation.

The HApFe suspension proved to be one of the most stable suspensions of those tested in recent years [42,43]. The stability parameter can be determined much faster than 5000 s for this particular suspension. In less than 1 min, the stability parameter reached a stable small value, proving the perfect stability of the suspension.

The resulting patterns for the HApFe nanocomposite powder and coating, as well as the reference peaks for pure hydroxyapatite (HAp) and maghemite (γ -Fe₂O₃), are shown in Figure 3. The peaks observed at 2θ angles in the XRD spectrum for the HApFe nanocomposite powder and coating correspond to the pure HAp (JCPD reference card 9-432). The peaks of γ -Fe₂O₃ (JCPD reference card 39-1346) are also presented in Figure 3a,b. In the present research, the values of calculated lattice constants of $a = b$ and c are 9.401 Å and 6.869 Å for powder and 9.398 and 6.867 Å for coatings. We can observe that the substitution of Fe ions for Ca sites in the HAp lattice causes a slight change in the lattice parameters “a” and “c” of the HApFe nanocomposite powder and coating samples compared to the lattice parameters of pure HAp ($a = b = 9.4166$ Å and $c = 6.8745$ Å). The lattice parameters of the HApFe nanocomposite powder and coating confirm the formation of iron-doped hydroxyapatite, as seen in the XRD profile and according to the literature [15,35,44–46]. The peaks associated with (002), (210), (211), (300), and (202) reflection planes were used in order to calculate the average crystal sizes of both samples. The values of the crystal sizes obtained for the analyzed samples (HApFe nanocomposite powder and coating) were 23.4 ± 0.5 nm and 18.7 ± 1 nm, respectively. In Figure 3, it can be seen that there is no individual peak that matches the γ -Fe₂O₃ peak, which shows that Fe²⁺/Fe³⁺ was substi-

tuted in HAp. The width of the peaks indicates that after the substitution of Ca^{2+} ions with $\text{Fe}^{2+}/\text{Fe}^{3+}$, the HApFe composite is more amorphous.

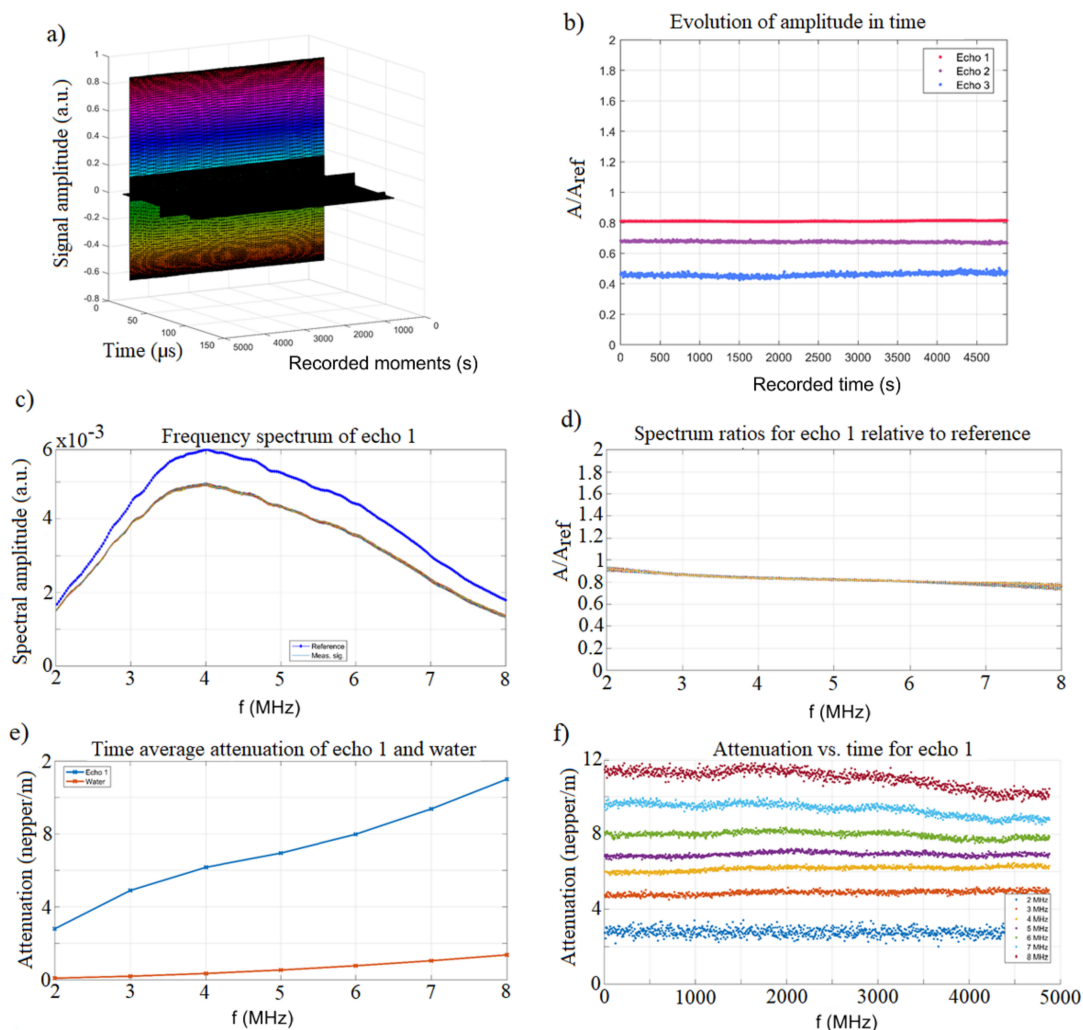


Figure 2. (a) Recorded signals at 5 s recording interval. The constant peak amplitudes of the first echo are shown in color, whereas the second and third echo are significantly weaker (shown in black). (b) Relative amplitudes of evolution vs. the recording moments. (c) Frequency spectrum of the first transmitted echo. Reference fluid (\blacklozenge). (d) Relative spectral amplitude (A/A_{ref}) vs. frequency. (e) Attenuation vs. frequency for the first transmitted echo. (f) Attenuation vs. time for the spectral components of the first echo.

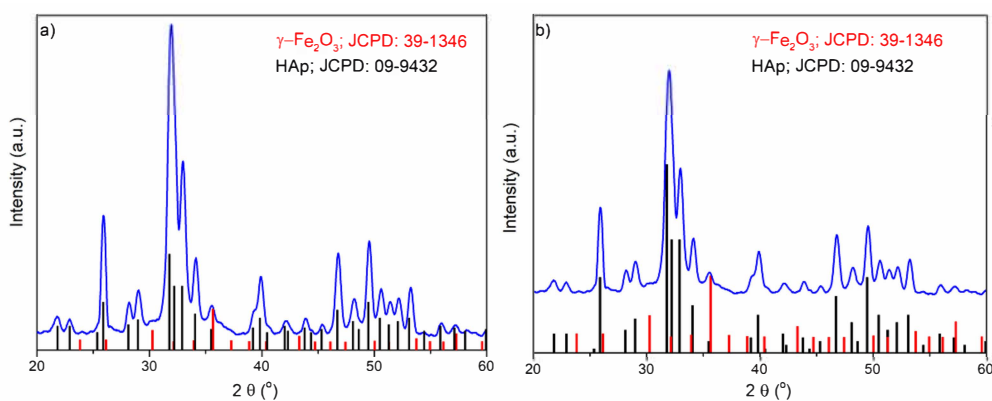


Figure 3. The XRD patterns of iron-doped hydroxyapatite (HApFe) (blue) powder (a) and coatings (b) and reference patterns for (black) HAp PDF #09-9434 and (red) Fe_2O_3 PDF # 39-1346.

The presence of iron in the HAp structure led to a decrease in the length of HAp particles. It can be seen that HApFe nanoparticles have an almost spherical shape (Figure 4a). The presence of iron in the HAp structure led to a decrease in the length of HAp particles. Thus, if in the case of pure HAp there are particles with an acicular or ellipsoidal shape [47–49], the nanoparticles will have an almost spherical shape. The average particle size (D_{TEM}) deduced from the particle size distribution of HApFe (Figure 4b) was 24 ± 1 nm. Information about the morphology and particle size are presented in Figure 4. It can be seen that HApFe nanoparticles have an almost spherical shape (Figure 4a). The existence of independent iron oxide particles was not noticed, which suggests that there was no free iron in the system. The TEM results are in good accordance with the XRD studies.

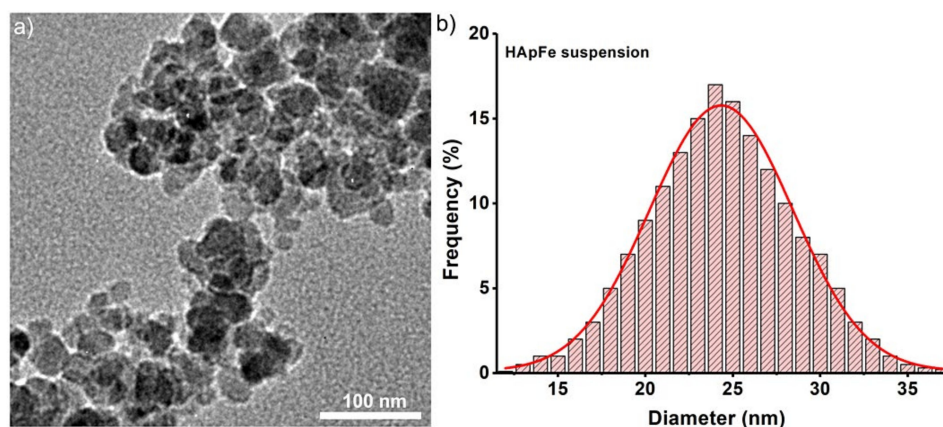


Figure 4. The TEM image of iron-doped hydroxyapatite (a) and the particle size distribution (b).

The HApFe particles and coatings were investigated regarding their morphologies and chemical compositions using scanning electron microscopy. The micrographs obtained using scanning electron microscopy, along with the EDS spectra and elemental distribution maps on HApFe particles and derived coatings, are presented in Figures 5 and 6. In the SEM images of HApFe particles, it can be observed that the sample consists of particles with nanometric dimensions (D_{SEM} is 25 ± 2 nm) and an almost spherical morphology (Figure 5). On the other hand, SEM studies have shown that HApFe coatings are homogeneous and continuous and contain no cracks on their surfaces (Figure 6).

The elemental composition and elemental distribution maps of HApFe particles and coatings were also assessed and are presented in Figures 5 and 6.

The chemical composition and elemental distribution maps of HApFe particles are presented in Figure 5d–h. In the EDS spectrum (Figure 5d), the presence of the main constituent chemical elements can be observed, namely calcium (Ca), phosphorus (P), oxygen (O), and iron (Fe). In Figure 5e–h, one can observe that the main constituent elements (Ca, P, O, and Fe) are uniformly distributed in the sample, proving their homogeneity and purity.

In the EDS spectra presented in Figure 6, it can be observed that in addition to the chemical elements mentioned above, in the case of HApFe coatings, the EDS spectrum highlights the presence of Si (from the substrate). The thickness of the HApFe coatings was around 150 nm. Additionally, Figure 6 shows that the HApFe coatings are homogeneous and pure. Moreover, the elemental distribution maps obtained on the HApFe coatings also highlight the presence of the main constituent elements (Ca, P, O, and Fe) and their uniform distribution on the surface, as well as the purity of the coatings (Figure 6).

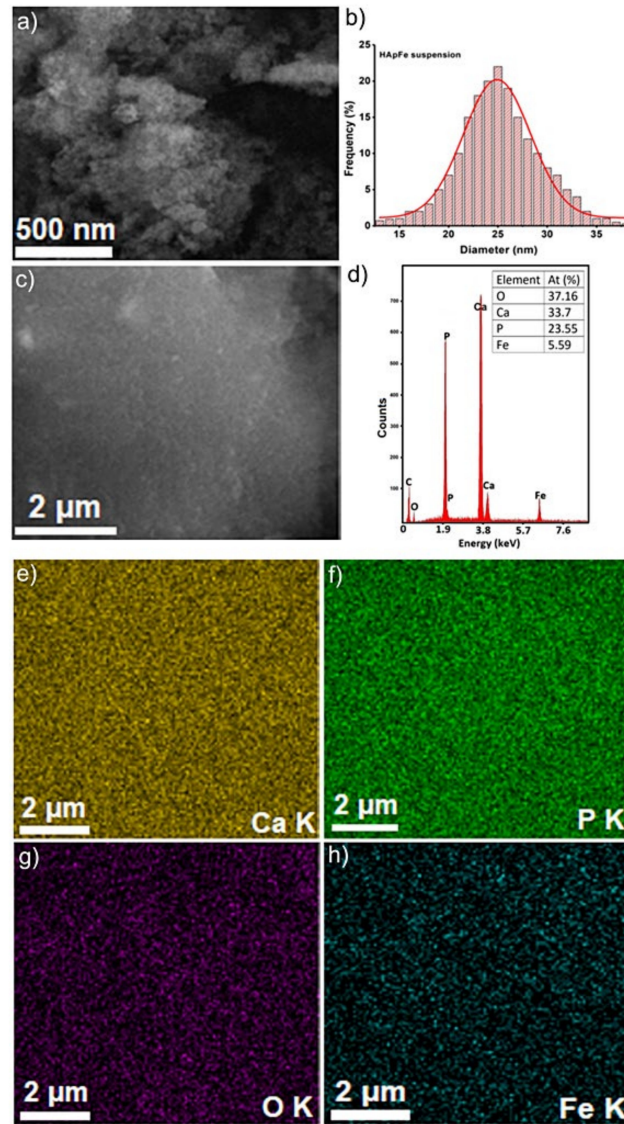


Figure 5. SEM micrographs of particle size distribution (a,b), SEM micrographs of elemental distribution (c), EDS spectra (d), and elemental distribution maps for Ca (e), P (f), O (g), and Fe (h) of HApFe particles.

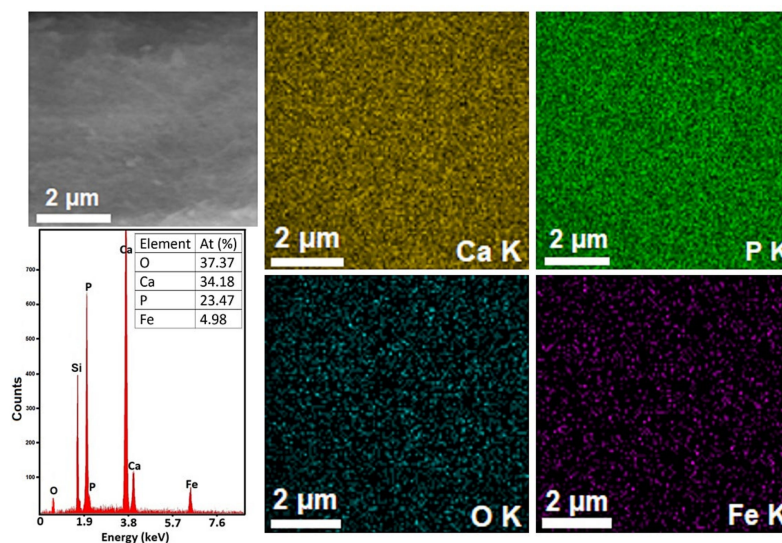


Figure 6. SEM micrographs of elemental distribution, EDS spectra, and elemental distribution maps of HApFe coatings.

Therefore, we can say that the SEM studies revealed that the purity of the samples was preserved in both the suspension and HApFe coatings. It can also be observed that the maxima associated with the main chemical elements constituting the EDS spectra were slightly more intense in the case of HApFe coatings compared to the HApFe suspension. The results obtained using SEM studies are in good agreement with the results obtained using XRD and TEM studies.

The surface topography of the HApFe coatings was examined using AFM analysis. Figure 7a,b shows the two-dimensional (2D) AFM topography of the HApFe coatings' surfaces over an area of $10 \times 10 \mu\text{m}^2$ and the three dimensional (3D) representation of the coatings' surfaces obtained using Image J software [39]. The 2D topography of the surface morphology of HApFe coatings showed that the HApFe coatings had a uniform morphology and did not show any cracks. Furthermore, no evidence of fissures or other defects were detected on the HApFe coatings' surfaces. Moreover, the 3D representation of the AFM image of the HApFe coatings' surfaces exhibited the morphology of a homogenous and uniformly deposited layer with aggregates of nanometric size. The results of the AFM topography also revealed that the HApFe coatings had a roughness (R_{RMS}) value of 120.83 nm.

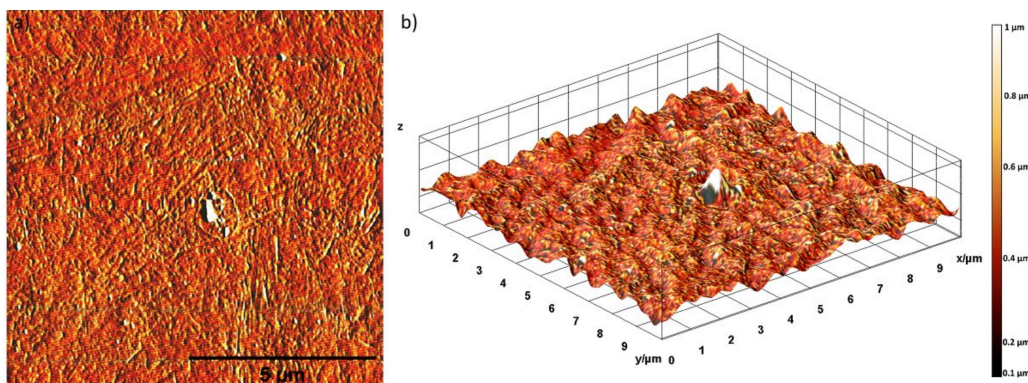


Figure 7. Topographical images of HApFe coatings (a) obtained using AFM and 3D representations of the topographical images of HApFe coatings (b).

The biocompatibility of the iron-doped hydroxyapatite (HApFe) suspensions and nanocomposite coatings was assessed by *in vitro* assay using osteoblast cells. The *in vitro* toxicity of the HApFe suspensions and coatings was investigated at different time intervals. A free culture grown at the tested time intervals was used as control. Furthermore, the cell viability of osteoblast cells was also investigated in the presence of Si discs used to obtain HApFe coatings. The results of the MTT (3-(4,5-Dimethylthiazol-2-yl)-2,5-Diphenyltetrazolium Bromide) assay regarding the cell viability of osteoblast cells incubated with the HApFe suspension and coatings are depicted in Figure 8. The MTT colorimetric standard assay is a laboratory test that measures changes in color in order to determine cellular proliferation. Yellow MTT (3-(4,5-Dimethylthiazol-2-yl)-2,5-diphenyltetrazolium bromide, a tetrazole) is reduced to purple formazan in the mitochondria of living cells. A solubilization solution (isopropanol) is added to dissolve the insoluble purple formazan product into a colored solution. The absorbance of this colored solution can be quantified by measuring it at a certain wavelength using a spectrophotometer. This reduction takes place only when mitochondrial reductase enzymes are active, and therefore conversion is directly related to the number of viable cells.

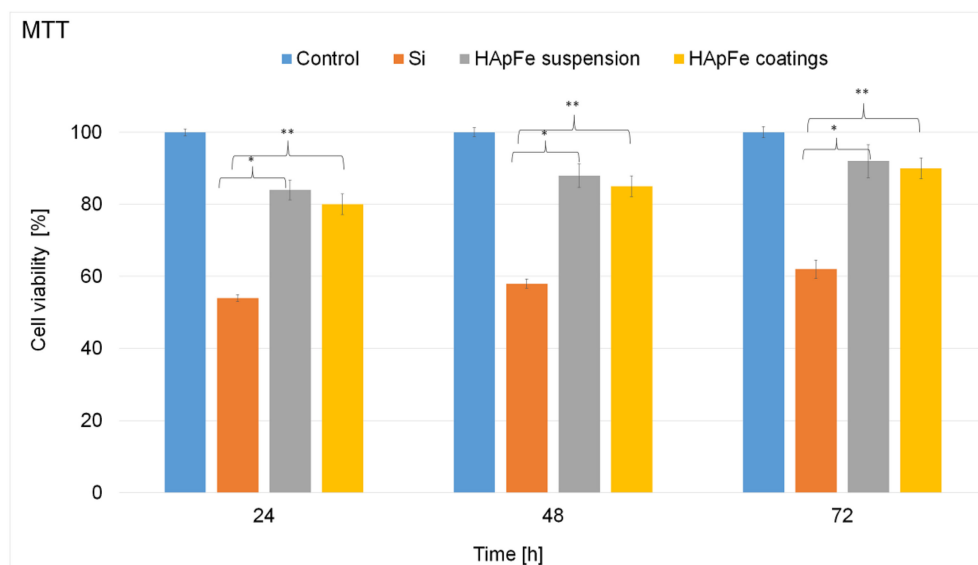


Figure 8. MTT assay of the viability of osteoblast cells incubated with Si discs and HApFe suspensions and coatings for 24, 48, and 72 h. Control is represented by an osteoblast cell culture grown on polystyrene Petri dish. The results are presented as means \pm standard error. The data were statistically analyzed using paired and two-sample *t*-tests for means, with $p \leq 0.05$ accepted as statistically significant (* $p \leq 0.005$; ** $p \leq 0.05$).

The results of the MTT analysis highlighted that both HApFe suspensions and coatings showed good cell viability, having values above 80%. In addition, the results of the cell viability assay demonstrated that there was no noticeable difference in the cell viability of the cells incubated with the HApFe suspensions and coatings. However, a slight increase in cell viability was observed in the case of HApFe suspensions compared to the HApFe coatings for all tested time periods compared to the control cells. The results of the MTT assay also showed that the Si discs reduced the cell viability of the osteoblast cells to under 80%. Moreover, the results also emphasized that the cell viability of the osteoblast cells was dependent not only on the samples, but also on the incubation time period.

The adhesion and proliferation of osteoblast cells on the surfaces of HApFe coatings was studied using AFM. AFM studies also provided information on cell morphology and spreading. For this purpose, the surfaces of HApFe coatings incubated with osteoblast cells for 24, 48, and 72 h were investigated using AFM topography [50]. In addition, the adhesion and proliferation of the osteoblast cells on the Si discs used in the development of HApFe coatings was also investigated using AFM after 24, 48, and 72 h of incubation. The results for the AFM surface topography of the Si discs and HApFe coatings incubated with osteoblast cells for 24, 48, and 72 h are presented in Figure 9a–l. By analyzing the results of the 2D AFM surface topography of the HApFe coatings incubated with osteoblast cells for 72 h (Figure 9k), it was observed that the cells adhered to the surfaces. Moreover, the results of the AFM studies showed that the cell adherence on the surfaces of HApFe coatings was better than on the surfaces of Si discs. In addition, the AFM topographies also emphasized that the cells adhered and proliferate better on the surfaces of HApFe coatings compared to the surfaces of Si discs for all the incubation time intervals. Furthermore, the data also suggested that the cellular viability was maintained after 72 h of incubation on the HApFe coatings, thus indicating that the surfaces of the HApFe coatings did not exert any cytotoxic effects on the osteoblast cell adhesion and proliferation. In addition, the 2D AFM image and the 3D representation of the AFM image of the HApFe coatings incubated with osteoblast cells for 24, 48, and 72 h emphasized that the HApFe coatings promoted the development of the osteoblast cells and provided a good adhesive surface compared to the Si discs.

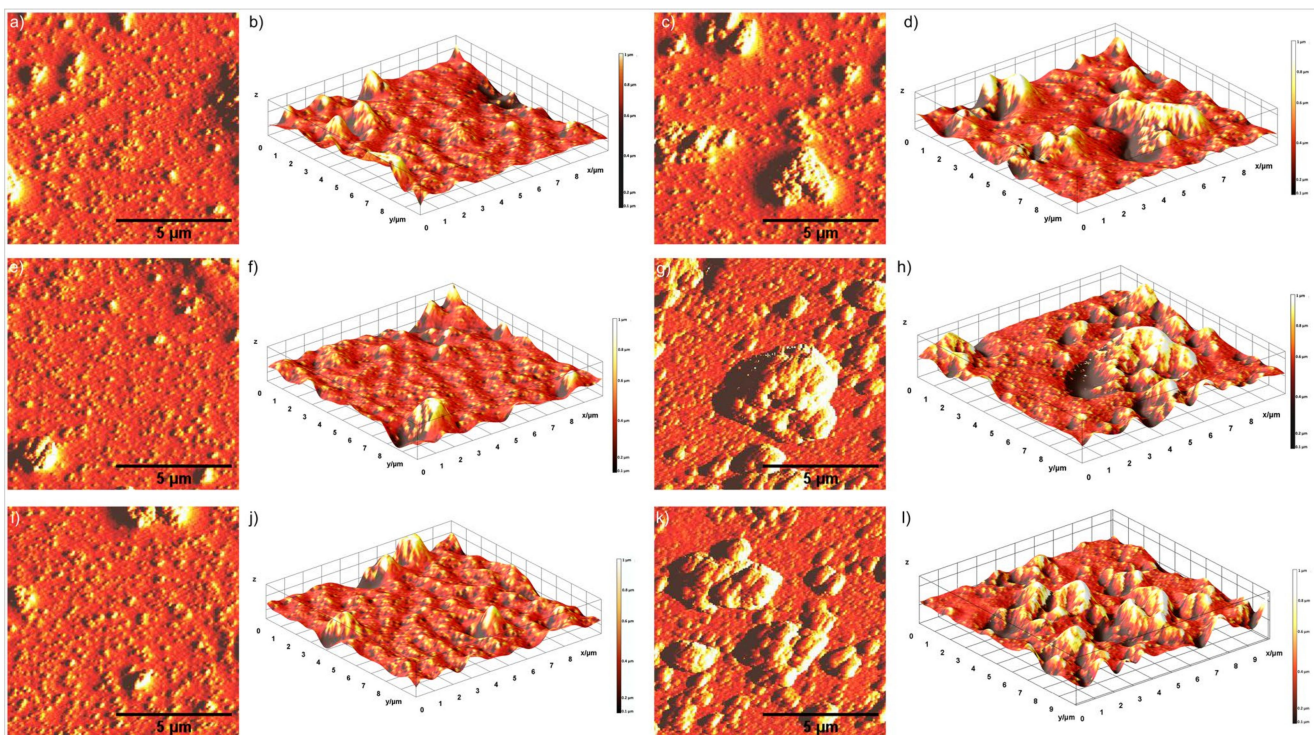


Figure 9. The 2D and 3D representations of the AFM surface topography of osteoblast cell development on Si after 24 h (a,b), 48 h (e,f), and 72 h (i,j) of incubation and on HApFe coatings after 24 h (c,d), 48 h (g,h), and 72 h (k,l) of incubation, collected across an area of $10 \times 10 \mu\text{m}^2$.

4. Discussion

In order to use the iron-doped HAp prepared using a co-precipitation protocol for the drug delivery system (DDS), the size and shape of the HApFe nanoparticles play important roles. Moreover, the stability of the suspensions is also very important. Despite the fact that the DLS technique can be used at different temperatures and concentrations, it does not allow the analysis of the concentrated suspension. By determining the ζ potential (ZP), we can gain information on the stability of the HApFe suspensions. The obtained value highlights the good stability [51]. Additionally, the value obtained for the ζ potential of the diluted suspension shows that the suspended particles were not agglomerated [52]. The results obtained regarding the ZP of the HApFe suspension were in good agreement with previous studies by Joseph and Singhvi [53], which proved that suspensions with ZP values of less than -30 mV or greater than 30 mV have high degrees of stability. Moreover, Shnoudeh et al. [54] showed that the magnitude of the ZP allows prediction of the colloidal stability. Previous studies [54] established that the ζ potential values of nanoparticles with values >25 mV or <-25 mV usually have high degrees of stability.

The new method based on ultrasonic measurements of the suspension obtained from the synthesis process allowed evaluation with better accuracy. The accuracy of the information comes from the fact that unlike the known techniques, this new technique that we developed allows us to evaluate the suspensions used in making the coatings in their concentrated forms. As with the coatings, the HApFe suspension analyzed using ultrasound measurements was stirred for 5 min before being analyzed. Measurements were made immediately after the suspension was stirred. Ultrasound measurement (US) revealed that the HApFe suspension showed very good stability compared to the reference fluid, which was double-distilled water. Our XRD patterns of iron-doped hydroxyapatite (HApFe) were in agreement with previous results regarding iron-doped hydroxyapatite [44–46]. As can be seen in Figure 3, the position of the peaks corresponds to the structure of hydroxyapatite. This behavior suggests that the structure of hydroxyapatite did not change after incorporating $\text{Fe}^{2+}/\text{Fe}^{3+}$. This result is in agreement with previous studies [55–58]. Our results are

in good agreement with the previous studies reported in the literature [57,59,60] regarding the morphology and chemical composition of iron-doped hydroxyapatite obtained using various techniques. The XRD results are in good agreement with the TEM and SEM studies. Determining the particle size and the size distribution as accurately as possible plays an important role in the characterization of nanomaterials. The different characterization techniques have contributed to highlighting specific properties for future applications in the medical field. The difference between the values obtained is due to the technique used. The slight difference between the average size values obtained may be due to the calculation of the size. In measuring the size distribution of TEM and SEM images, some differences may occur in the XRD results due to the ability of image processing algorithms to separate particles that are in contact with each other. Although TEM is considered the gold standard technique for determining the size of nanoparticles, it is, however, limited because it gives little information about the shell around a nanoparticle's core. XRD and SEM also provide information on the metal cores of nanoparticles only. Following the XRD and SEM studies, information was provided on the particle core, because after drying the coating the metal core was destroyed. Dynamic light scattering (DLS) results include both the metal core and the surface coating molecules and a sphere of hydration around the nanoparticles, compared to usually only the metal core being reported in traditional TEM size measurements [61]. This explains the high values obtained for the hydrodynamic diameter of the nanoparticles (a diameter that includes both the particle core and the surface coating) using DLS analysis. The TEM studies have shown that the shape of HApFe nanoparticles (almost spherical) is due to the doping of hydroxyapatite with iron ions. The TEM results obtained in this study are in agreement with our previous studies, which have shown that both the dopant and the method influence the size and shape of nanoparticles [47–49]. In studies on the synthesis and antimicrobial activity of silver-doped hydroxyapatite nanoparticles, the results suggested that doping with Ag⁺ had little influence on the size of HAp nanoparticles [47]. On the other hand, in studies evaluating the antibacterial activity of zinc-doped hydroxyapatite colloids and dispersion stability using ultrasounds, the particles had a slightly elongated shape [49]. Moreover, the studies on removal of zinc ions using hydroxyapatite and on the ultrasound behavior of aqueous media revealed almost spherical particles [48].

The MTT assay highlighted that both samples had very good biocompatibility. The cell viability of the osteoblast cells incubated with HApFe suspensions and coatings was above 80% in the first 24 h and increased with incubation time. In addition, the results of the MTT assay also highlighted that the HApFe coatings presented better biocompatible properties than the Si discs. The results suggested that the HApFe samples had significant biocompatible properties, which were in good agreement with previous studies regarding the hydroxyapatite properties facilitating the attachment and growth of osteoblast cells [62]. The slight decrease of cell viability compared with the control (100%) could be attributed to the cells' adaptation to the interactions with the samples. The osteoblast cell viability values were significantly lower ($p < 0.005$ and $p < 0.05$, respectively) on Si than on HApFe coatings for all the studied time intervals. These results demonstrated that the HApFe coatings promote the proliferation of osteoblast cells.

The results of the MTT in vitro assay highlighted that there is a correlation between the incubation time and the cell viability of the samples, both in the case of HApFe suspensions and coatings. The cell viability of the osteoblast cells incubated with the HApFe suspensions and coatings exhibited a slight increase with the incubation time. Moreover, the MTT suggested that the suspensions exhibited better biocompatible properties than the coatings for all tested incubation periods. The results obtained in the present study are in good agreement with previously reported studies regarding the toxicity of hydroxyapatite suspensions and coatings on different cell types [63,64].

Recently, the AFM technique was reported as a novel method for high-resolution imaging of any surface, including those of living and fixed cells [65]. Therefore, the adhesion of the osteoblast cells on the surface of HApFe coatings was also assessed using

atomic force microscopy and scanning electron microscopy. The osteoblast cells were permanently monitored to detect any possible influence of the HApFe coatings that might modify the cell growth, viability, and proliferation.

In this context, the SEM and AFM studies of the HApFe samples demonstrated that the surface morphology and topography were uniform and that the constituent elements were homogeneously distributed in the samples, thus achieving a suitable support for the development of biomedical devices. Our previous studies on silver-ion-doped hydroxyapatite [11,47,66] demonstrated the antimicrobial potential of these materials and highlighted the influence of the silver concentration on the antimicrobial properties by highlighting the minimum inhibitory concentration and active concentration of biofilms on microbial strains such as Gram-positive *Bacillus subtilis*, *Staphylococcus aureus* 0364, and *Enterococcus faecalis* ATCC 29212; Gram-negative *Escherichia coli* ATCC 25922, *Klebsiella pneumoniae* 2968, *Enterobacter cloacae* 61R, and *Pseudomonas aeruginosa* 1397; and yeast (*Candida krusei* 963). On the other hand, recent studies regarding materials based on lavender essential oil and hydroxyapatite [67] have shown that lavender essential oil significantly improves the antimicrobial properties of hydroxyapatite, even at low concentrations. Furthermore, studies on the synthesis, characterization, and antimicrobial activity of magnesium-doped hydroxyapatite suspensions [43] provided additional information on the stability of MgHAp nanoparticle suspensions synthesized using an adapted chemical co-precipitation method, which allowed us to obtain biocompatible coatings. All of these studies [11,43,47,66,67] have helped in the understanding of some of the mechanisms of antimicrobial activity of materials based on hydroxyapatite doped with different ions, which may contribute to the development of new antimicrobial agents that are needed to combat the phenomena of antibiotic resistance. On the other hand, these studies have provided important information on the surfaces of implantable materials, contributing to the identification of alternative solutions that can facilitate improved interactions between calcium phosphate and bone mineral implants [11,43,47,66,67]. Previous studies have also reported the existence of active interactions between cells and surfaces on nanostructured surfaces, even at the early stage of adhesion. In their studies, Dalby et al. [68] reported that fibroblast cells extended their filopodia and interacted with 95 nm islands faster than those on plane control surfaces within 30 min, while Sato et al. [69] reported for the first time a study demonstrating that Y-doped nanocrystalline HA coatings on titanium promoted calcium deposition by using osteoblasts over plasma-sprayed HA coatings.

The results of the current study may contribute to the development of technologies that could have positive effects on the interactions between biomedical materials and cells and biomolecules. In this way, strategies can be developed for the design and manufacture of intelligent materials with specific functionalities that could be used to treat and remedy diseases, such as those of the skeletal system.

5. Conclusions

The present study shows that HApFe particles could be successfully synthesized to be used in various medical applications, such as for coverings of certain implants. Iron was incorporated into the HAp structure during the synthesis by using an adapted co-precipitation method, which was performed at room temperature. The stability of the HApFe nanocomposite suspension was certified by DLS and ultrasound measurements. The peaks identified in the XRD spectrum for the HApFe nanocomposite powder and coating were associated with pure HAp. A slight change in the lattice parameters “*a*” and “*c*” was observed after the HAp was doped with iron ions. The average particle size deduced from the particle size distribution of the HApFe shown in the TEM image ($D_{\text{TEM}} = 24 \pm 1$ nm) was in accordance with the average size calculated from the XRD studies ($D_{\text{XRD}} = 23.4 \pm 0.5$ nm) and the SEM image ($D_{\text{SEM}} = 25 \pm 2$ nm). TEM and SEM analyses revealed that HApFe has an almost spherical shape. Impurities or independent iron oxide particles were not observed following studies performed by XRD, TEM, and

SEM analyses. The uniform distribution of the constituent elements (Ca, P, O, and Fe) in the samples was confirmed by elemental distribution maps.

The AFM studies of the surface morphology of the HApFe coatings showed that the morphology was uniform, without showing any cracks, fissures, or discontinuities. The MTT in vitro cytotoxicity assays also demonstrated that both HApFe suspensions and coatings showed good biocompatibility on osteoblast cells. Furthermore, the osteoblast cells' proliferation and adhesion on the surface of the HApFe coatings was also demonstrated by AFM analysis. The results of the biological assays showed that the HApFe samples did not affect the viability and proliferation of the osteoblast cells at any of the tested time intervals. Moreover, the in vitro studies also suggested that the HApFe coatings promoted the proliferation and adhesion of the osteoblast cells after 72 h of incubation compared to the Si discs. The MTT assays also highlighted that the cell viability of the osteoblast cells incubated with HApFe coatings was significantly better than the cell viability of the Si discs for all the tested time intervals.

Taking into account both the physico-chemical and biological properties of HApFe coatings and suspensions, we can say that they can be used successfully in future biomedical applications (including for tissue engineering, prosthetics, etc.).

Author Contributions: Conceptualization, D.P., M.B., and S.L.I.; methodology, D.P., S.L.I., S.C.C., M.B., S.-A.P., C.M., and N.B.; software, S.-A.P.; validation, D.P., S.L.I., M.B., S.C.C., C.M., and N.B.; formal analysis, D.P., S.L.I., M.B., S.C.C., S.-A.P., C.M., and N.B.; investigation, D.P., S.L.I., M.B., S.C.C., S.-A.P., C.M., and N.B.; resources, D.P., S.L.I., M.B., S.C.C., C.M., and N.B.; data curation, S.L.I. and S.-A.P.; writing—original draft preparation, D.P., S.L.I., S.-A.P., M.B., S.C.C., C.M., and N.B.; writing—review and editing, D.P., S.L.I., S.C.C., and S.-A.P.; visualization, D.P., S.L.I., M.B., S.C.C., S.-A.P., C.M., and N.B.; supervision, D.P., S.L.I., M.B., C.M., and N.B.; project administration, M.B.; funding acquisition, M.B. All authors have read and agreed to the published version of the manuscript.

Funding: This research was partially funded by the Romanian Ministry of Research and Innovation with the grant and project No. PN-III-P1-1.2-PCCDI-2017-0629 and contract NO. 43PCCDI/2018, respectively.

Data Availability Statement: The samples are not available.

Acknowledgments: We thank Annie Richard and Audrey Sauldubois from the “Centre de Microscopie Electronique” of University of Orléans for assistance in SEM data acquisition. This work was supported by the Romanian Ministry of Research and Innovation through project No. PN-III-P1-1.2-PCCDI-2017-0629/contract No. 43PCCDI/2018 and Core Program PN19-030101 (contract 21N/2019).

Conflicts of Interest: The authors declare no conflict of interest.

References

1. Cai, W.; Chen, X. Nanoplatfoms for targeted molecular imaging in living subjects. *Small* **2007**, *3*, 1840–1854. [[CrossRef](#)] [[PubMed](#)]
2. Martina, M.S.; Fortin, J.P.; Ménager, C.; Clément, O.; Barratt, G.; Grabielle-Madelmont, C.; Gazeau, F.; Cabuil, V.; Lesieur, S. Generation of superparamagnetic liposomes revealed as highly efficient MRI contrast agents for in vivo imaging. *J. Am. Chem. Soc.* **2005**, *127*, 10676–10685. [[CrossRef](#)]
3. Gupta, A.K.; Curtis, A.S.G. Surface modified superparamagnetic nanoparticles for drug delivery: Interaction study with human fibroblast in culture. *J. Mater. Sci. Mater. Med.* **2004**, *15*, 493–496. [[CrossRef](#)]
4. Gupta, A.K.; Gupta, M. Synthesis and surface engineering of iron oxide nanoparticles for biomedical applications. *Biomaterials* **2005**, *26*, 3995–4021. [[CrossRef](#)] [[PubMed](#)]
5. Davis, M.E.; Chen, Z.G.; Shin, D.M. Nanoparticle therapeutics: An emerging treatment modality for cancer. *Nat. Rev. Drug Discov.* **2008**, *7*, 771–782. [[CrossRef](#)] [[PubMed](#)]
6. Zhang, L.; Gu, F.X.; Chan, J.M.; Wang, A.Z.; Langer, R.S.; Farokhzad, O.C. Nanoparticles in medicine: Therapeutic applications and developments. *Clin. Pharmacol. Ther.* **2008**, *83*, 761–769. [[CrossRef](#)]
7. Peer, D.; Karp, J.; Hong, S.; Farokhzad, O.C.; Margalit, R.; Langer, R. Nanocarriers as an emerging platform for cancer therapy. *Nat. Nanotechnol.* **2007**, *2*, 751–760. [[CrossRef](#)] [[PubMed](#)]
8. Song, N.; Liu, Y.; Zhang, Y.; Tan, Y.N.; Grover, L.M. Synthesis and characterisation of iron substituted apatite. *Adv. Appl. Ceram.* **2012**, *111*, 466–471. [[CrossRef](#)]
9. Suchanek, W.; Yoshimura, M. Processing and properties of hydroxyapatite-based biomaterials for use as hard tissue replacement implants. *J. Mater. Res.* **1998**, *13*, 94–117. [[CrossRef](#)]

10. Kuriakose, T.; Kalkura, S.; Palanichamy, M.; Arivuoli, D.; Dierks, K.; Bocelli, G.; Betzel, C. Synthesis of stoichiometric nano crystalline hydroxyapatite by ethanol-based sol–gel technique at low temperature. *J. Cryst. Growth* **2004**, *263*, 517–523. [[CrossRef](#)]
11. Costescu, A.; Ciobanu, C.S.; Iconaru, S.L.; Ghita, R.V.; Chifiriuc, C.M.; Marutescu, L.G.; Predoi, D. Fabrication, characterization, and antimicrobial activity, evaluation of low silver concentrations in silver-doped hydroxyapatite nanoparticles. *J. Nanomater.* **2013**, *2013*, 194854. [[CrossRef](#)]
12. Predoi, D.; Predoi, M.V.; Iconaru, S.L.; Ech Cherif El Kettani, M.; Leduc, D.; Prodan, A.M. Ultrasonic measurements on β cyclodextrin/hydroxyapatite composites for potential water depollution. *Materials* **2017**, *10*, 681. [[CrossRef](#)] [[PubMed](#)]
13. Predoi, D.; Iconaru, S.L.; Predoi, M.V. Fabrication of silver- and zinc-doped hydroxyapatite coatings for enhancing antimicrobial effect. *Coatings* **2020**, *10*, 905. [[CrossRef](#)]
14. Negrila, C.C.; Predoi, M.V.; Iconaru, S.L.; Predoi, D. Development of zinc-doped hydroxyapatite by sol-gel method for medical applications. *Molecules* **2018**, *23*, 2986. [[CrossRef](#)] [[PubMed](#)]
15. Panseri, S.; Cunha, C.; D’Alessandro, T.; Sandri, M.; Giavaresi, G.; Marcacci, M.; Hung, C.T.; Tampier, A. Intrinsically superparamagnetic Fe-hydroxyapatite nanoparticles positively influence osteoblast-like cell behaviour. *J. Nanobiotechnol.* **2012**, *10*, 32. [[CrossRef](#)] [[PubMed](#)]
16. Mondal, S.; Manivasagan, P.; Bharathiraja, S.; Santha Moorthy, M.; Kim, H.H.; Seo, H.; Lee, K.D.; Oh, J. Magnetic hydroxyapatite: A promising multifunctional platform for nanomedicine application. *Int. J. Nanomed.* **2017**, *12*, 8389–8410. [[CrossRef](#)] [[PubMed](#)]
17. Parelman, M.; Stoecker, B.; Baker, A.; Medeiros, D. Iron restriction negatively affects bone in female rats and mineralization of hFOB osteoblast cells. *Exp. Biol. Med.* **2006**, *231*, 378–386. [[CrossRef](#)]
18. Singh, S.; Singh, G.; Bala, N. Synthesis and characterization of iron oxide-hydroxyapatite-chitosan composite coating and its biological assessment for biomedical applications. *Prog. Org. Coat.* **2021**, *150*, 106011. [[CrossRef](#)]
19. Raynal, I.; Prigent, P.; Peyramaure, S.; Najid, A.; Rebuzzi, C.; Corot, C. Macrophage endocytosis of superparamagnetic iron oxide nanoparticles: Mechanisms and comparison of ferumoxides and ferumoxtran-10. *Investig. Radiol.* **2004**, *39*, 56–63. [[CrossRef](#)]
20. Sarath Chandra, V.; Baskar, G.; Suganthi, R.V.; Elayaraja, K.; Ahymah Joshy, M.I.; Sofi Beaula, W.; Mythili, R.; Venkatraman, G.; Narayana Kalkura, S. Blood compatibility of iron-doped nanosize hydroxyapatite and its drug release. *ACS Appl. Mater. Interfaces* **2012**, *4*, 1200–1210. [[CrossRef](#)]
21. Ajeesh, M.; Francis, B.F.; Annie, J.; Varma, P.R.H. Nano iron oxide-hydroxyapatite composite ceramics with enhanced radiopacity. *J. Mater. Sci. Mater. Med.* **2010**, *21*, 1427–1434. [[CrossRef](#)]
22. Pareta, R.A.; Taylor, E.; Webster, T.J. Increased osteoblast density in the presence of novel calcium phosphate coated magnetic nanoparticles. *Nanotechnology* **2008**, *19*, 265101. [[CrossRef](#)]
23. Russo, A.; Bianchi, M.; Sartori, M.; Boi, M.; Giavaresi, G.; Salter, D.M.; Jelic, M.; Maltarello, M.C.; Ortolani, A.; Sprio, S.; et al. Bone regeneration in a rabbit critical femoral defect by means of magnetic hydroxyapatite macroporous scaffolds. *J. Biomed. Mater. Res. Part B* **2018**, *106B*, 546–554. [[CrossRef](#)]
24. Panseri, S.; Russo, A.; Sartori, M.; Giavaresi, G.; Sandri, M.; Fini, M.; Maltarello, M.C.; Shelyakova, T.; Ortolani, A.; Visani, A.; et al. Modifying bone scaffold architecture in vivo with permanent magnets to facilitate fixation of magnetic scaffolds. *Bone* **2013**, *56*, 432–439. [[CrossRef](#)] [[PubMed](#)]
25. Morrissey, R.; Rodrigue-Lorenzo, L.M.; Gross, K.A. Influence of ferrous iron incorporation on the structure of hydroxyapatite. *J. Mater. Sci. Mater. Med.* **2005**, *16*, 387–392. [[CrossRef](#)]
26. Wu, H.C.; Wang, T.W.; Sun, J.S.; Wang, W.H.; Lin, F.H. A novel biomagnetic nanoparticle based on hydroxyapatite. *Nanotechnology* **2007**, *18*, 165601. [[CrossRef](#)]
27. Murakami, S.; Hosono, T.; Jeyadevan, B.; Kamitakahara, M.; Ioku, K. Hydrothermal synthesis of magnetite/hydroxyapatite composite material for hyperthermia therapy for bone cancer. *J. Am. Ceram. Soc.* **2008**, *116*, 950–954. [[CrossRef](#)]
28. Donadel, K.; Felisberto, M.D.V.; Laranjei, M.C.M. Preparation and characterization of hydroxyapatite-coated iron oxide particles by spray-drying technique. *An. Acad. Bras. Ciênc.* **2009**, *81*, 179–186. [[CrossRef](#)] [[PubMed](#)]
29. Vucinic Vasic, M.; Antic, B.; Boškovic, M.; Antic, A.; Blanuša, J. Hydroxyapatite/iron oxide nanocomposite prepared by high energy ball milling. *Process. Appl. Ceram.* **2019**, *13*, 210–217. [[CrossRef](#)]
30. Klein, C.P.; Blicck-Hogemrst, J.M.A.; Wolket, J.G.C.; Groot, K.D. Studies of the solubility of different calcium phosphate ceramic particles in vitro. *Biomaterials* **1990**, *11*, 509–512. [[CrossRef](#)]
31. Singh, S.; Singh, G.; Bala, N. Electrophoretic deposition of hydroxyapatite-iron oxide-chitosan composite coatings on Ti–13Nb–13Zr alloy for biomedical applications. *Thin Solid Film.* **2020**, *697*, 137801. [[CrossRef](#)]
32. Huang, Y.; Ding, Q.; Han, S.; Yan, Y.; Pang, X. Characterisation, corrosion resistance and in vitro bioactivity of manganese-doped hydroxyapatite films electrodeposited on titanium. *J. Mater. Sci. Mater. Med.* **2013**, *24*, 1853–1864. [[CrossRef](#)] [[PubMed](#)]
33. Singh, R.K.; Srivastava, M.; Prasad, N.K.; Awasthi, S.; Dhayalan, A.; Kannan, S. Iron doped β -Tricalcium phosphate: Synthesis, characterization, hyperthermia effect, biocompatibility and mechanical evaluation. *Mater. Sci. Eng. C Mater. Biol. Appl.* **2017**, *78*, 715–726. [[CrossRef](#)] [[PubMed](#)]
34. Ramana Ramya, J.; Thanigai Arul, K.; Elayaraja, K.; Narayana Kalkura, S. Physicochemical and biological properties of iron and zinc ions co-dopednanocrystalline hydroxyapatite, synthesized by ultrasonication. *Ceram. Int.* **2014**, *40*, 16707–16717. [[CrossRef](#)]
35. Tampieri, A.; D’Alessandro, T.; Sandri, M.; Sprio, S.; Landi, E.; Bertinetti, L.; Panseri, S.; Pepponi, G.; Goettlicher, J.; Bañobre-López, M.; et al. Intrinsic magnetism and hyperthermia in bioactive Fe-doped hydroxyapatite. *Acta Biomater.* **2012**, *8*, 843–851. [[CrossRef](#)]
36. Rodriguez, L.; Matoušek, J. Preparation of TiO₂ sol-gel layers on glass. *Ceram. Silik.* **2003**, *47*, 28–31.

37. Prodan, A.M.; Iconaru, S.L.; Predoi, M.V.; Predoi, D.; Motelica-Heino, M.; Turculet, C.S.; Beuran, M. Silver-doped hydroxyapatite thin layers obtained by sol-gel spin coating procedure. *Coatings* **2020**, *10*, 14. [CrossRef]
38. Patterson, A. The scherrer formula for x-ray particle size determination. *Phys. Rev.* **1939**, *56*, 978–982. [CrossRef]
39. ImageJ Website. Available online: <http://imagej.nih.gov/ij> (accessed on 10 January 2020).
40. Gwyddion. Available online: <http://gwyddion.net/> (accessed on 20 January 2020).
41. Predoi, D.; Iconaru, S.L.; Predoi, M.V. Bioceramic layers with antifungal properties. *Coatings* **2018**, *8*, 276. [CrossRef]
42. Predoi, D.; Iconaru, S.L.; Predoi, M.V.; Stan, G.E.; Buton, N. Synthesis, characterization, and antimicrobial activity of magnesium-doped hydroxyapatite suspensions. *Nanomaterials* **2019**, *9*, 1295. [CrossRef]
43. Gallagher, A.J.; Gundle, R.; Beresford, N.J. Isolation and Culture of Bone-Forming Cells (Osteoblasts) from Human Bone. In *Human Cell Culture Protocols. Methods in Molecular Medicine*; Jones, G.E., Ed.; Humana Press: Totowa, NJ, USA, 1996; Volume 2, pp. 233–263. [CrossRef]
44. Tran, N.; Webster, T.J. Increased osteoblast functions in the presence of hydroxyapatite-coated iron oxide nanoparticles. *Acta Biomater.* **2011**, *7*, 1298–1306. [CrossRef] [PubMed]
45. Ansar, E.B.; Ajeesh, M.; Yokogawa, Y.; Wunderlich, W.; Varma, H. Synthesis and characterization of iron oxide embedded hydroxyapatite bioceramics. *J. Am. Ceram. Soc.* **2012**, *95*, 2695–2699. [CrossRef]
46. Li, Y.; Nam, C.T.; Ooi, C.P. Iron(III) and manganese(II) substituted hydroxyapatite nanoparticles: Characterization and cytotoxicity analysis. *J. Phys. Conf. Ser.* **2009**, *187*, 012024. [CrossRef]
47. Ciobanu, C.S.; Iconaru, S.L.; Chifiriuc, M.C.; Costescu, A.; Le Coustumer, P.; Predoi, D. Synthesis and antimicrobial activity of silver-doped hydroxyapatite nanoparticles. *Biomed. Res. Int.* **2013**, *2013*, 916218. [CrossRef] [PubMed]
48. Iconaru, S.L.; Motelica-Heino, M.; Guegan, R.; Predoi, M.V.; Prodan, A.M.; Predoi, D. Removal of zinc ions using hydroxyapatite and study of ultrasound behavior of aqueous media. *Materials* **2018**, *11*, 1350. [CrossRef] [PubMed]
49. Predoi, D.; Iconaru, S.L.; Predoi, M.V.; Motelica-Heino, M.; Guegan, R.; Buton, N. Evaluation of antibacterial activity of zinc-doped hydroxyapatite colloids and dispersion stability using ultrasounds. *Nanomaterials* **2019**, *9*, 515. [CrossRef] [PubMed]
50. Kuznetsova, T.G.; Starodubtseva, M.N.; Yegorenkov, N.I.; Chizhik, S.A.; Zhdanov, R.I. Atomic force microscopy probing of cell elasticity. *Micron* **2007**, *38*, 824–833. [CrossRef] [PubMed]
51. Kadu, P.J.; Kushare, S.S.; Thacker, D.D.; Gattani, S.G. Enhancement of oral bioavailability of atorvastatin calcium by self-emulsifying drug delivery systems (SEDDS). *Pharm. Dev. Technol.* **2011**, *16*, 65–74. [CrossRef]
52. Mohapatra, S.S.; Ranjan, S.; Thomas, S. *Characterization and Biology of Nanomaterials for Drug Delivery Nanoscience and Nanotechnology in Drug Delivery*, 1st ed.; Elsevier: San Diego, CA, USA, 2019. [CrossRef]
53. Joseph, E.; Singhvi, G. Multifunctional nanocrystals for cancer therapy: A potential nanocarrier. In *Nanomaterials for Drug Delivery and Therapy*, 1st ed.; Grumezescu, A.M., Ed.; Elsevier: San Diego, CA, USA, 2019; pp. 91–116. [CrossRef]
54. Shnoudeh, A.J.; Hamad, I.; Abdo, R.W.; Qadumii, L.; Jaber, A.Y.; Surchi, H.S.; Alkelany, S.Z. Synthesis, characterization, and applications of metal nanoparticles, biomaterials and bionanotechnology. In *Advances in Pharmaceutical Product Development and Research*; Tekade, R.K., Ed.; Academic Press: San Diego, CA, USA, 2019; pp. 527–612. [CrossRef]
55. Mercado, D.F.; Magnacca, G.; Malandrino, M.; Rubert, A.; Montoneri, E.; Celi, L.; Bianco Prevot, A.; Gonzalez, M.C. Paramagnetic iron-doped hydroxyapatite nanoparticles with improved metal sorption properties. a bioorganic substrates-mediated synthesis. *ACS Appl. Mater. Interfaces* **2014**, *6*, 3937–3946. [CrossRef]
56. Kramer, E.R.; Morey, A.M.; Staruch, M.; Suib, S.L.; Jain, M.; Budnick, J.I.; Wei, M. Synthesis and characterization of iron-substituted hydroxyapatite via a simple ion-exchange procedure. *J. Mater. Sci.* **2013**, *48*, 665–673. [CrossRef]
57. Jiang, M.; Terra, J.; Rossi, A.M.; Morales, M.A.; Baggio Saitovitch, E.M.; Ellis, D.E. Fe²⁺/Fe³⁺ substitution in hydroxyapatite: Theory and experiment. *Phys. Rev. B Condens. Matter Mater. Phys.* **2002**, *66*, 2241071–22410715. [CrossRef]
58. Wang, J.; Nonami, T.; Yubata, K. Synthesis, structure and photophysical properties of iron containing hydroxyapatite prepared by a modified pseudo-body solution. *J. Mater. Sci. Mater. Med.* **2008**, *19*, 2663–2667. [CrossRef]
59. Raua, J.V.; Cacciotti, I.; De Bonis, A.; Fosca, M.; Komlev, V.S.; Latini, A.; Santagata, A.; Teghil, R. Fe-doped hydroxyapatite coatings for orthopedic and dental implant applications. *Appl. Surf. Sci.* **2014**, *307*, 301–305. [CrossRef]
60. Pon-On, W.; Meejoo, S.; Tang, I.-M. Incorporation of iron into nano hydroxyapatite particles synthesized by the microwave process. *Int. J. Nanosci.* **2007**, *6*, 9–16. [CrossRef]
61. MacCuspie, R.I.; Rogers, K.; Patra, M.; Suo, Z.; Allen, A.J.; Martin, M.N.; Hackley, V.A. Challenges for physical characterization of silver nanoparticles under pristine and environmentally relevant conditions. *J. Environ. Monit.* **2011**, *13*, 1212–1226. [CrossRef] [PubMed]
62. Thian, E.S.; Ahmad, Z.; Huang, J.; Edirisinghe, M.J.; Jayasinghe, S.N.; Ireland, D.C.; Brooks, R.A.; Rushton, N.; Bonfield, W.; Best, S.M. The role of surface wettability and surface charge of electrosprayed nanoapatites on the behaviour of osteoblasts. *Acta Biomater.* **2010**, *6*, 750–755. [CrossRef] [PubMed]
63. Cai, Y.L.; Zhang, J.J.; Zhang, S.; Venkatraman, S.S.; Zeng, X.T.; Du, H.J.; Mondal, D. Osteoblastic cell response on fluoridated hydroxyapatite coatings: The effect of magnesium incorporation. *Biomed. Mater.* **2010**, *5*, 054114. [CrossRef] [PubMed]
64. Oliveira, A.L.; Mano, J.F.; Reis, R.L. Nature-inspired calcium phosphate coatings: Present status and novel advances in the science of mimicry. *Curr. Opin. Solid State Mater. Sci.* **2003**, *7*, 309–318. [CrossRef]
65. Bischoff, G.; Hein, H.-J. *Micro- and Nanostructures of Biological Systems*, 1st ed.; Shaker: Aachen, Germany, 2003.

66. Ciobanu, C.S.; Massuyeau, F.; Constantin, L.V.; Predoi, D. Structural and physical properties of antibacterial Ag-doped nano-hydroxyapatite synthesized at 100 °C. *Nanoscale Res. Lett.* **2011**, *6*, 613. [[CrossRef](#)]
67. Predoi, D.; Iconaru, S.L.; Buton, N.; Badea, M.L.; Marutescu, L. Antimicrobial activity of new materials based on lavender and basil essential oils and hydroxyapatite. *Nanomaterials* **2018**, *8*, 291. [[CrossRef](#)]
68. Dalby, M.J.; Childs, S.; Riehle, M.O.; Johnstone, H.J.H.; Affrossman, S.; Curtis, A.S.G. Fibroblast reaction to island topography: Changes in cytoskeleton and morphology with time. *Biomaterials* **2003**, *24*, 927–935. [[CrossRef](#)]
69. Sato, M.; Sambito, M.A.; Aslani, A.; Kalkhoran, N.M.; Slamovich, E.B.; Webster, T.J. Increased osteoblast functions on undoped and yttrium-doped nanocrystalline hydroxyapatite coatings on titanium. *Biomaterials* **2006**, *27*, 2358–2369. [[CrossRef](#)] [[PubMed](#)]